Non-Line-of-Sight Imaging and Vibrometry Using a Comb-Calibrated Coherent Sensor

Xin Huang,[1,2,*] Ruilin Ye,[1,2,*] Wenwen Li,[1,2,3,*] Jian-Wei Zeng[1,2] Yi-Chen Lu,[1,2] Huiqin Hu[1,2] Yijun Zhou,[1,2]
Lei Hou,[1,2,3] Zheng-Ping Li,[1,2,3] Hai-Feng Jiang,[1,2,3] Xianghui Xue,[1,3,4] Feihu Xu[1,2,3,†]
Xiankang Dou,[1,3,4,‡] and Jian-Wei Pan[1,2,3,§]

[1]*Hefei National Research Center for Physical Sciences at the Microscale and School of Physical Sciences,*
University of Science and Technology of China, Hefei 230026, China
[2]*Shanghai Research Center for Quantum Science and CAS Center for Excellence in Quantum Information and Quantum Physics,*
University of Science and Technology of China, Shanghai 201315, China
[3]*Hefei National Laboratory, University of Science and Technology of China, Hefei 230088, China*
[4]*School of Earth and Space Science, University of Science and Technology of China, Hefei 230026, China*

Non-line-of-sight (NLOS) imaging has the ability to reconstruct hidden objects, allowing a wide range of applications. Existing NLOS systems rely on pulsed lasers and time-resolved single-photon detectors to capture the information encoded in the time of flight of scattered photons. Despite remarkable advances, the pulsed time-of-flight LIDAR approach has limited temporal resolution and struggles to detect the frequency-associated information directly. Here, we propose and demonstrate the coherent scheme— frequency-modulated continuous wave calibrated by optical frequency comb—for high-resolution NLOS imaging, velocimetry, and vibrometry. Our comb-calibrated coherent sensor presents a system temporal resolution at subpicosecond and its superior signal-to-noise ratio permits NLOS imaging of complex scenes under strong ambient light. We show the capability of NLOS localization and 3D imaging at submillimeter scale and demonstrate NLOS vibrometry sensing at an accuracy of dozen Hertz. Our approach unlocks the coherent LIDAR techniques for widespread use in imaging science and optical sensing.

Introduction.—Non-line-of-sight (NLOS) imaging has the capability to image objects that are hidden from a camera's direct view [1,2]. A variety of NLOS imaging methods have been proposed and demonstrated, including speckle correlations [3–5], time-of-flight (TOF) light detection and ranging (LIDAR) [6–13], phasor field [14,15], wavefront shaping [16,17], and others [18–20]. Among these, the TOF-LIDAR approach is considered as one of the most promising directions toward practical solutions [6–15,21–28]. Leveraging short-pulsed lasers and time-resolved single-photon detectors [29,30], TOF-LIDAR systems can reveal the 3D structure of hidden objects at centimeter-scale resolution [9–15]. However, further improving the image resolution is challenging because the temporal resolution of the pulsed TOF-LIDAR systems is normally limited to around tens of picoseconds [9–15,21–25]. Furthermore, the pulsed TOF-LIDAR approach cannot directly detect the frequency-associated information such as the vibration. Note that the capability to measure the microamplitude periodic motion, i.e., vibrometry sensing, is of great interest in general areas ranging from industrial monitoring [31] and voice recognition [32] to clinical measurements [33,34].

Our ambition to achieve high-resolution NLOS imaging and vibrometry motivates the use of the coherent scheme—frequency-modulated continuous wave (FMCW). FMCW-LIDAR employs a swept laser as the transmitter to emit frequency-modulated light, and uses an interferometric detection as the receiver to detect the back-reflected signals [35–37]. This coherent scheme offers the unique advantages of high-resolution ranging and imaging [38–40], direct vibration measurement [41,42], and the resistance to environment noise [43]. FMCW-LIDAR has recently attracted considerable attention for line-of-sight applications [44–47]. Nonetheless, the straight translation to NLOS scenario is not feasible, as the diffuse nature of light reflected from typical surfaces in NLOS imaging leads to mixing of spatial information and low signal-to-noise ratio (SNR) in the collected light, seemingly precluding useful scene reconstruction.

Here, we demonstrate a coherent scheme to tackle NLOS imaging and sensing problems and employ an optical frequency comb (OFC) [48] to realize high-resolution NLOS 3D imaging, velocimetry, and vibrometry. The comb-calibrated method can improve the sensor's SNR by ∼5 dB, permitting useful NLOS scene reconstruction. Our coherent sensor presents a temporal resolution of 652 fs, which can be enhanced to 70 fs using a broader-tuning-bandwidth laser [38,49,50]. We demonstrate NLOS localization of hidden object at a resolution of 150 μm and 3D imaging for complex hidden scenes at a resolution of millimeter scale. Furthermore, we show the capability of velocimetry and vibrometry sensing by resolving the audio signals of a hidden speaker ranging from 1 to 8 kHz with a vibration frequency accuracy of ∼15 Hz.
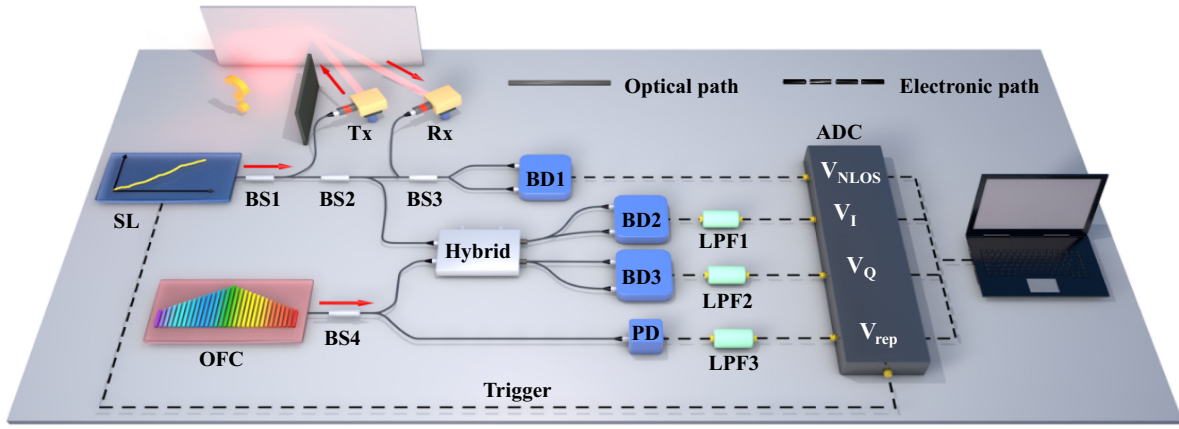
FIG. 1. The experimental setup. A quasi-linearly-chirped swept laser (SL) probes the hidden objects through the transceiver. The confocal transceiver illuminates (Tx) and detects (Rx) at the same point and raster-scans across the visible wall. The returned signal at each scanning point is captured by a balanced detector (BD) and a digitizer. Simultaneously, an OFC is used to monitor the instantaneous frequency of the swept laser through a 90° optical hybrid. The in-phase–quadrature (IQ) signals and the repetition rate of the OFC are recorded. BS, beam splitter; PD, photodiode; LPF, low-pass filter; ADC, analog-to-digital converter.

Principle.—We explain the concept in a confocal scanning configuration [11]. An optical transceiver illuminates and detects the same point and raster-scans across the visible relay wall. At each scanning point, a tunable laser is quasilinearly chirped with a sweep rate of γ and a nonlinear term $k(t)$, so its frequency can be written as

$$f_{\rm L}(t) = \gamma t + f_0 + k(t), \tag{1}$$

where f_0 is the initial laser frequency. The corresponding electric field of the laser output can be written as $e^{i\varphi(t)}$, where the phase component $\varphi(t) = 2\pi \int_0^t f_{\rm L}(t)(\tau)d\tau$ and the amplitude of the field is set to 1 for simplicity. If we discretize the surfaces of the hidden targets to $n_x \times n_y$ pixels, each pixel (x, y) will contribute to the returned signal as $E_{xy}e^{i\varphi(t-\Delta t_{xy})}$. Here, E_{xy} depends on the reflectivity of pixel (x, y), and the path attenuation between the scanning point and this pixel. Δt_{xy} is the propagation time of light between these two points. By summing up all the pixels on the hidden objects, the returned signal collected by the receiver can be written as $\sum_{x,y} E_{xy}e^{i\varphi(t-\Delta t_{xy})}$. This returned signal is compared to the local oscillator $e^{i\varphi(t)}$ via an interferometric measurement using balanced detection. The balanced detection output $V_{\rm NLOS}(t)$, which can be represented as the sum of the comparison between each pixel and the local oscillator, is given by (Supplemental Material, Sec. I and Sec. III [51])

$$V_{\rm NLOS}(t) \propto \sum_{x,y} E_{xy} \cos(\varphi(t) - \varphi(t - \Delta t_{xy}))$$
$$\overset{(a)}{\approx} \sum_{x,y} E_{xy} \cos\left(\frac{d\varphi(t)}{dt}\Delta t_{xy}\right)$$
$$= \sum_{x,y} E_{xy} \cos\left(2\pi \Delta t_{xy} \cdot f_{\rm L}(t)\right), \tag{2}$$

where (a) follows the linear approximation. If $f_{\rm L}(t)$ itself is treated as the argument, by performing fast Fourier transform (FFT) on $V_{\rm NLOS}(f_{\rm L})$, TOF information Δt_{xy} and attenuation information E_{xy} can be extracted. Then, 3D structure of the hidden scene can be inferred using state-of-art computational algorithms [11–14].

For vibrometry sensing, suppose the hidden target is vibrating at a certain frequency $f_{\rm v}$. Through the same sensing procedure, our system captures the vibration-associated measurement $V'_{\rm NLOS}(t)$ at a single point on the wall. A series of evenly spaced peaks will arise in the FFT result. By calculating the spacing between the neighboring peaks, the vibration frequency can be estimated [Supplemental Material, Eqs. (S3) and (S12) [51]].

OFC calibration: An OFC is adopted to track the instantaneous frequency $f_{\rm L}(t)$. One portion of the swept laser is calibrated against the OFC through in-phase–quadrature (IQ) demodulation (Supplemental Material, Fig. S4). In IQ demodulation, the relative frequency evolution between the swept laser and the nearest comb tooth can be determined, which corresponds to the laser frequency approaching, crossing, and moving away from the individual comb tooth. This calibration effectively eliminates the frequency fluctuation of the swept laser. In practice, the laser is chirped with inevitable fluctuations, i.e., $k(t) \neq 0$ in Eq. (1), and an unexpected term $\Delta t_{xy}k(t)$ will be introduced. We then treat $f_{\rm L}(t)$ itself rather than t as the argument. We find OFC calibration can effectively suppress the spectrum broadening effect by ~1000 fold (Supplemental Material, Sec. III and Table S2 [51]).

Setup.—Our setup is depicted in Fig. 1. A tunable external cavity laser (Luna, PHOENIX 1200) is quasilinearly chirped with a maximum excursion bandwidth of 2 THz (from 1541 to 1557 nm). The laser power is set at 10 mW and the output is split into three portions by two

beam splitters BS1 and BS2 (90∶10). The first portion (9 mW) is sent to hidden scenes through the transmitter (Tx) while the second portion (0.9 mW) is used as the local oscillator. The light reflected back is collected by the receiver (Rx). Both Tx and Rx consist of a galvo mirror and a collimator. The returned light is mixed with the local oscillator at BS3 (50∶50) and detected by a balanced detector BD1. The detector output $V_{\mathrm{NLOS}}(t)$ is captured with a 16-bit 1 GS/s digitizer.

The third portion of the laser output (0.1 mW) is compared to a homemade OFC to track its instantaneous frequency. This portion is mixed with the comb output via a 90° optical hybrid. The IQ outputs of the hybrid are detected with BD2 and BD3. The detector outputs, filtered by two low-pass filters LPF1 and LPF2, are recorded with the digitizer as $V_{\mathrm{I}}(t)$ and $V_{\mathrm{Q}}(t)$. Besides, the repetition rate of the comb is detected by a photodiode, filtered by LPF3 and recorded with the digitizer as $V_{\mathrm{rep}}(t)$.

The homemade comb centered around 1550 nm is generated by a passively mode-locked Er fiber laser based on a nonlinear amplifying loop mirror [67]. The output power of comb is about 1 mW and the carrier-envelope offset frequency f_{ceo} is set to 163.9 MHz. The repetition rate f_{r} is 200.3 MHz, or equivalently, the frequency separation of the comb tooth.

Reconstruction.—The reconstruction is to resample V_{NLOS} in laser frequency domain and extract NLOS information from the resampled signal. First, a complex signal $V_{\mathrm{IQ}} = V_{\mathrm{I}} + iV_{\mathrm{Q}}$ is constructed. The phase of V_{IQ} is given by calculating and unwrapping $\arctan(V_{\mathrm{Q}}/V_{\mathrm{I}})$. The instantaneous frequency $f_{\mathrm{L}}(t)$ is determined by the derivation of this phase. With it, V_{NLOS} is resampled (see Supplemental Material, Sec. IV and Fig. S5 [51]). Second, we perform FFT on the resampled signals at each scanning point and square the results. With these pixelwise squared results, a 3D matrix is constructed and the hidden scene can be reconstructed by applying transient NLOS imaging algorithms [11,12,14]. Note that the FFT results give the amplitude distribution over the arrival time, while the transient measurements give the intensity distribution. Thus we square the FFT results before the reconstruction using transient algorithms. Finally, a find-peaks program is performed on the FFT result. We locate the vibration-associated peaks and calculate the spacing between neighboring peaks. As this spacing is determined by f_{v}/γ, the recovered frequency is obtained by scaling the calculated spacing with the sweep rate γ.

Results.—Temporal resolution: The transmitter and receiver of the setup are coupled to a variable optical delay line (VODL) through polarization-maintaining fibers. We set VODL to 0 μm and the tuning bandwidth of the swept laser to 1 THz. The ranging results with and without comb are given in Fig. 2(a). The full width at half maximum (FWHM) of the temporal response can be reduced from ~500 to 1.2 ps with the equipment of the comb, almost
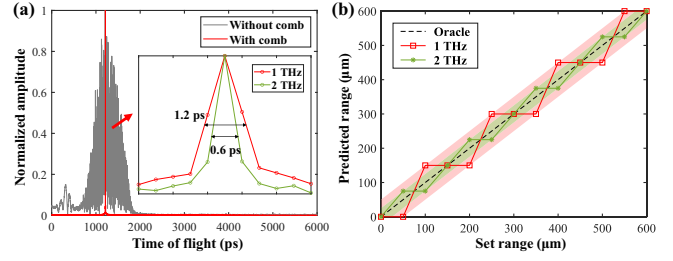
FIG. 2. Temporal resolution test. (a) Temporal results at 0 μm. Without comb calibration, the full width at half maximum (FWHM) of the temporal response is ~500 ps; with comb, it almost reaches the theoretical limit determined by the bandwidths (1 ps for 1 THz and 0.5 ps for 2 THz). (b) Ranging results. The system operating at 1 THz (2 THz) bandwidth offers a ranging deviation of 50 μm (25 μm).

reaching the theoretical resolution limit (1 ps) determined by the 1 THz bandwidth. Moreover, 2 THz tuning bandwidth is tested, and a resolution of 651.9 fs is achieved, approaching the theory limit of 500 fs. Note that the temporal resolution can be enhanced to ~70 fs by further extending the tuning range of the swept laser and the spectrum range of the comb [50,68]. We then move VODL from 0 to 600 μm with a minimum step of 50 μm. The comb-calibrated ranging results over this series of displacements are presented in Fig. 2(b). When operating at 1 THz bandwidth, our system can offer a ranging deviation of 50 μm. And this deviation is reduced to 25 μm with 2 THz bandwidth.

NLOS imaging: A rough white wall is confocally scanned at 128×128 locations over a $15\ \mathrm{cm} \times 15\ \mathrm{cm}$ region. A hidden scenes are placed about ~15 to 20 cm away from it, consisting of four items with different depths: a drop of water (5 mm), a letter "H" (10 mm), a number "7" (15 mm), and a Chinese character "Zhong" (20 mm). At each scanning location, we typically set the acquisition time to 10 ms and the tuning bandwidth to 1 THz (Supplemental Material, Table S3 [51]). Figure 3(a) exhibits its NLOS signals at a scanning point, including the reflections of relay wall and hidden objects. This indicates that the comb calibration can not only reduce the temporal broadening, but also enhance the SNR by ~5 dB. Figure 4(c) presents the reconstruction result of hidden scene, where the 5 mm spacing can be resolved. Figure S10 in the Supplemental Material shows the reconstruction result of another complex scene. Figures S7 and S8 in the Supplemental Material show results for two resolution charts, where the lateral resolution can reach 5 mm and the axial resolution can reach 2 mm.

Imaging resolution: The imaging resolution of the NLOS system depends on several aspects including the geometry [11], the temporal resolution and the structure of the relay wall [20] (Supplemental Material, Sec. VI [51]). By adopting an aluminum wall and 1 THz tuning bandwidth, we demonstrate NLOS localization at the resolution
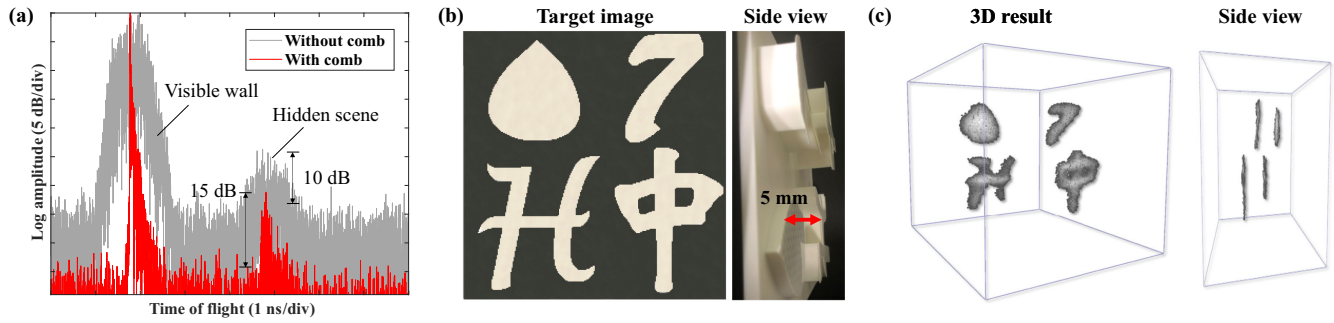
FIG. 3.   NLOS imaging. (a) NLOS signals with and without the comb calibration. The comparison indicates that the comb calibration can both reduce the temporal broadening and improve the signal-to-noise ratio (SNR) by ∼5 dB. (b) Ground truth of the hidden objects. (c) The reconstructed images with and without the comb calibration. The 5 mm spacing can be resolved with our comb-calibrated FMCW sensor.

of 150 µm (Supplemental Material, Fig. S11 [51]). Although other experiments have shown the ability of NLOS imaging at sub-mm scale [5,7,20], our approach retains the distinctive advantages of high range ambiguity, single-photon sensitivity, and immunity to ambient light (Supplemental Material, Table S5 [51]). When a rough wall is employed instead, the system temporal response is broadened to ∼10 ps, leading to an imaging resolution at millimeter scale. This arises from the surface roughness of the wall, which introduces a degree of spread in the light propagation path [20]. We remark that our sub-ps system possesses the capability to precisely characterize the temporal broadening waveform induced by different wall surfaces (Supplemental Material, Fig. S7 [51]). This waveform data could potentially be harnessed for general applications including imaging through strongly diffusive mediums [69], lensless imaging [70], and wavefront shaping [17].

NLOS vibrometry and velocimetry: In our vibrometry experiments, the visible wall is sampled at a single point. The acquisition time is set to 200 ms, providing the spectrum resolution σ of 5 Hz. A commercial speaker, placed about 15 cm away from the visible wall, is driven from 1 to 8 kHz. Figure 4(a) exhibits the recovered NLOS signal without and with the comb calibration. Without the

comb-calibrated resampling method, broadening effect seriously blurs the vibration signals, while some equidistant vibration-associated peaks appear with the comb calibration, from which the vibration frequency can be recovered. Figure 4(b) visualizes the recovered vibrometry signals at $f_v = 2093$ Hz (do), 2637 Hz (mi), and 3136 Hz (so), respectively. The horizontal axis has been scaled to frequency domain, and the vibration frequency can be directly estimated by calculating the spacing between the neighboring peaks. Figure 4(c) shows that our setup can recover the frequency from 2 to 6 kHz with accuracy of ∼15 Hz (green error bar), within the empirical 3σ rule. We extend our testing range from 1 to 8 kHz, and comprehensively analyze our system's vibrometry capabilities (Supplemental Material, Sec. VII and Fig. S12 [51]). With similar experimental settings, we demonstrate NLOS velocimetry for moving objects (Supplemental Material, Sec. VIII and Fig. S13 [51]).

Discussion.—Compared to pulsed TOF methods, our coherent-based FMCW-LIDAR scheme presents several notable advantages (see Supplemental Material, Sec. II [51]). First, it stands out for its remarkable temporal resolution, resulting in the superior image quality. Most pulsed TOF schemes grapple with temporal resolutions in the range of tens of picoseconds limited by the detector
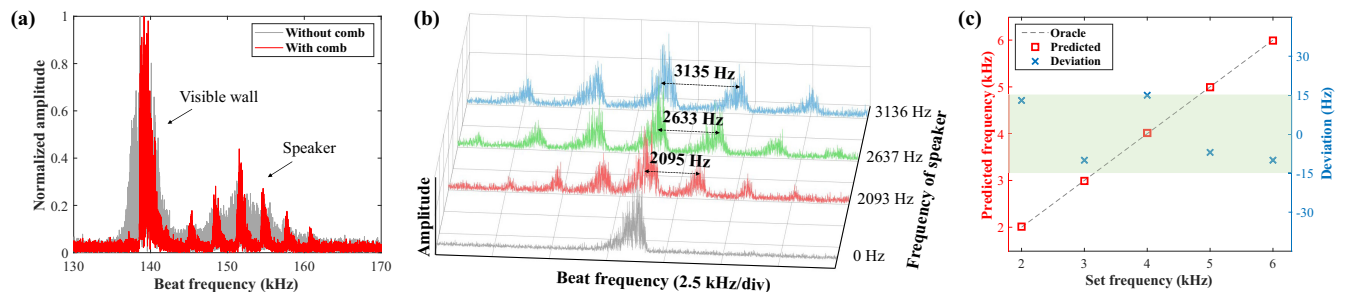
FIG. 4.   NLOS vibrometry. (a) Recovered vibration signals with and without comb calibration. (b) Visualization of the recovered NLOS vibrometry signals at some representative frequencies. (c) A series of tested frequencies, ranging from 2 to 6 kHz. Results show that the deviation is within 15 Hz (green bar).

bandwidth [9–15,21–25]. In contrast, FMCW circumvents this limit by using a swept-frequency optical waveform. With the laser's tuning range capable of spanning 15 THz, the temporal resolution could reach 70 fs, enabling image resolution below 10 μm [50]. Second, the frequency scheme is immune against background noise, which is a well-known characteristic of FMCW-LIDAR systems [71]. This inherent immunity to ambient light has been demonstrated in extreme scenarios like imaging through flames [43]. Third, our scheme possesses an uncommon ability of the *direct* detection of vibrations and velocity. While a TOF scheme has shown this capability by translating the frequency measurement into intensity measurement [27], FMCW scheme performs vibrometry in the frequency domain directly. By detecting the Doppler frequency shift, we demonstrate the vibrometry at a minimum amplitude of ∼9.7 nm and a maximum frequency of 8 kHz. Compared with the previous effort [27], our method extends the detection range of amplitude and frequency by ∼10 fold. Fourth, our FMCW scheme enables *snapshot* velocimetry. This allows the simultaneous measurement of the velocity and position of hidden objects in a single shot, without the need of accumulation over time. Lastly, recent advancements in chip-based FMCW-LIDAR have showcased significant progress in both industry and academia [44,45,47]. These developments provide strong technical support for more affordable and stable hardware solutions, which aligns with our vision for compact and accessible NLOS imaging systems.

*These authors contributed equally to this work.
†Corresponding author: feihuxu@ustc.edu.cn
‡Corresponding author: dou@ustc.edu.cn
§Corresponding author: pan@ustc.edu.cn

[1] Y. Altmann, S. McLaughlin, M. J. Padgett, V. K. Goyal, A. O. Hero, and D. Faccio, Science **361**, eaat2298 (2018).

[2] D. Faccio, A. Velten, and G. Wetzstein, Nat. Rev. Phys. **2**, 318 (2020).

[3] J. Bertolotti, E. G. Van Putten, C. Blum, A. Lagendijk, W. L. Vos, and A. P. Mosk, Nature (London) **491**, 232 (2012).

[4] O. Katz, P. Heidmann, M. Fink, and S. Gigan, Nat. Photonics **8**, 784 (2014).

[5] C. A. Metzler, F. Heide, P. Rangarajan, M. M. Balaji, A. Viswanath, A. Veeraraghavan, and R. G. Baraniuk, Optica **7**, 63 (2020).

[6] A. Kirmani, T. Hutchison, J. Davis, and R. Raskar, *Proceedings of the 2009 IEEE 12th International Conference on Computer Vision* (IEEE, New York, 2009), pp. 159–166.

[7] A. Velten, T. Willwacher, O. Gupta, A. Veeraraghavan, M. G. Bawendi, and R. Raskar, Nat. Commun. **3**, 1 (2012).

[8] F. Heide, L. Xiao, W. Heidrich, and M. B. Hullin, in *Proceedings of the IEEE/CVF Conference on Computer Vision and Pattern Recognition* (2014), pp. 3222–3229, https://www.cv-foundation.org/openaccess/content_cvpr_2014/html/Heide_Diffuse_Mirrors_3D_2014_CVPR_paper.html.

[9] M. Buttafava, J. Zeman, A. Tosi, K. Eliceiri, and A. Velten, Opt. Express **23**, 20997 (2015).

[10] M. Laurenzis, J. Klein, E. Bacher, and N. Metzger, Opt. Lett. **40**, 4815 (2015).

[11] M. O'Toole, D. B. Lindell, and G. Wetzstein, Nature (London) **555**, 338 (2018).

[12] D. B. Lindell, G. Wetzstein, and M. O'Toole, ACM Trans. Graph. **38**, 1 (2019).

[13] S. Xin, S. Nousias, K. N. Kutulakos, A. C. Sankaranarayanan, S. G. Narasimhan, and I. Gkioulekas, in *Proceedings of the IEEE/CVF Conference on Computer Vision and Pattern Recognition* (2019), pp. 6800–6809, https://openaccess.thecvf.com/content_CVPR_2019/html/Xin_A_Theory_of_Fermat_Paths_for_Non-Line-Of-Sight_Shape_Reconstruction_CVPR_2019_paper.html.

[14] X. Liu, I. Guillén, M. La Manna, J. H. Nam, S. A. Reza, T. Huu Le, A. Jarabo, D. Gutierrez, and A. Velten, Nature (London) **572**, 620 (2019).

[15] J. H. Nam, E. Brandt, S. Bauer, X. Liu, M. Renna, A. Tosi, E. Sifakis, and A. Velten, Nat. Commun. **12**, 1 (2021).

[16] A. P. Mosk, A. Lagendijk, G. Lerosey, and M. Fink, Nat. Photonics **6**, 283 (2012).

[17] R. Cao, F. de Goumoens, B. Blochet, J. Xu, and C. Yang, Nat. Photonics **16**, 462 (2022).

[18] F. Xu, G. Shulkind, C. Thrampoulidis, J. H. Shapiro, A. Torralba, F. N. Wong, and G. W. Wornell, Opt. Express **26**, 9945 (2018).

[19] C. Saunders, J. Murray-Bruce, and V. K. Goyal, Nature (London) **565**, 472 (2019).

[20] F. Willomitzer, P. V. Rangarajan, F. Li, M. M. Balaji, M. P. Christensen, and O. Cossairt, Nat. Commun. **12**, 6647 (2021).

[21] W. Chen, F. Wei, K. N. Kutulakos, S. Rusinkiewicz, and F. Heide, ACM Trans. Graph. **39**, 1 (2020).

[22] G. Gariepy, F. Tonolini, R. Henderson, J. Leach, and D. Faccio, Nat. Photonics **10**, 23 (2016).

[23] S. Chan, R. E. Warburton, G. Gariepy, J. Leach, and D. Faccio, Opt. Express **25**, 10109 (2017).

[24] C. Wu, J. Liu, X. Huang, Z.-P. Li, C. Yu, J.-T. Ye, J. Zhang, Q. Zhang, X. Dou, V. K. Goyal, F. Xu, and J.-W. Pan, Proc. Natl. Acad. Sci. U.S.A. **118**, e2024468118 (2021).

[25] X. Liu, J. Wang, Z. Li, Z. Shi, X. Fu, and L. Qiu, Light **10**, 1 (2021).

[26] B. Wang, M.-Y. Zheng, J.-J. Han, X. Huang, X.-P. Xie, F. Xu, Q. Zhang, and J.-W. Pan, Phys. Rev. Lett. **127**, 053602 (2021).

[27] S. Zhu, Y. M. Sua, P. Rehain, and Y.-P. Huang, Opt. Express **29**, 40865 (2021).

[28] S. Zhu, Y. M. Sua, T. Bu, and Y.-P. Huang, Phys. Rev. Appl. **19**, 034090 (2023).

[29] R. H. Hadfield, J. Leach, F. Fleming, D. J. Paul, C. H. Tan, J. S. Ng, R. K. Henderson, and G. S. Buller, Optica **10**, 1124 (2023).

[30] Z.-P. Li, J.-T. Ye, X. Huang, P.-Y. Jiang, Y. Cao, Y. Hong, C. Yu, J. Zhang, Q. Zhang, C.-Z. Peng *et al.*, Optica **8**, 344 (2021).

[31] S. Wagner and A.-V. Pham, in *2020 17th European Radar Conference (EuRAD)* (IEEE, New York, 2021), pp. 82–85.

[32] J. Zhang, Y. Zhou, R. Xi, S. Li, J. Guo, and Y. He, *Proceedings of the ACM on Interactive, Mobile, Wearable and Ubiquitous Technologies* (2022), Vol. 6, p. 1, https://dl.acm.org/doi/abs/10.1145/3550320.

[33] Y. Rong and D. W. Bliss, in *Proceedings of the 2019 IEEE Radar Conference (RadarConf)* (IEEE, New York, 2019), pp. 1–6.

[34] Z. Zhang, Y. Liu, T. Stephens, and B. J. Eggleton, Nat. Photonics **17**, 791 (2023).

[35] D. Uttam and B. Culshaw, J. Lightwave Technol. **3**, 971 (1985).

[36] E. Strzelecki, D. Cohen, and L. Coldren, J. Lightwave Technol. **6**, 1610 (1988).

[37] M.-C. Areann, T. Bosch, M. Lescure, A. Myllylae, and M. Rioux, Opt. Eng. **40**, 10 (2001), https://ui.adsabs.harvard.edu/abs/2001OptEn..40...10A/abstract.

[38] P. A. Roos, R. R. Reibel, T. Berg, B. Kaylor, Z. W. Barber, and W. R. Babbitt, Opt. Lett. **34**, 3692 (2009).

[39] F. Giorgetta, I. Coddington, E. Baumann, W. Swann, and N. Newbury, Nat. Photonics **4**, 853 (2010).

[40] E. Baumann, F. R. Giorgetta, J.-D. Deschênes, W. C. Swann, I. Coddington, and N. R. Newbury, Opt. Express **22**, 24914 (2014).

[41] W. Zhang, W. Gao, L. Huang, D. Mao, B. Jiang, F. Gao, D. Yang, G. Zhang, J. Xu, and J. Zhao, Opt. Express **23**, 17576 (2015).

[42] S. Suyama, H. Ito, R. Kurahashi, H. Abe, and T. Baba, Opt. Express **29**, 30727 (2021).

[43] E. W. Mitchell, M. S. Hoehler, F. R. Giorgetta, T. Hayden, G. B. Rieker, N. R. Newbury, and E. Baumann, Optica **5**, 988 (2018).

[44] J. Riemensberger, A. Lukashchuk, M. Karpov, W. Weng, E. Lucas, J. Liu, and T. J. Kippenberg, Nature (London) **581**, 164 (2020).

[45] C. Rogers, A. Y. Piggott, D. J. Thomson, R. F. Wiser, I. E. Opris, S. A. Fortune, A. J. Compston, A. Gondarenko, F. Meng, X. Chen, G. T. Reed, and N. Remus, Nature (London) **590**, 256 (2021).

[46] I. Kim, R. J. Martins, J. Jang, T. Badloe, S. Khadir, H.-Y. Jung, H. Kim, J. Kim, P. Genevet, and J. Rho, Nat. Nanotechnol. **16**, 508 (2021).

[47] X. Zhang, K. Kwon, J. Henriksson, J. Luo, and M. C. Wu, Nature (London) **603**, 253 (2022).

[48] S. A. Diddams, K. Vahala, and T. Udem, Science **369**, eaay3676 (2020).

[49] S.-H. Yun, C. Boudoux, G. J. Tearney, and B. E. Bouma, Opt. Lett. **28**, 1981 (2003).

[50] S. H. Yun, G. J. Tearney, B. J. Vakoc, M. Shishkov, W. Y. Oh, A. E. Desjardins, M. J. Suter, R. C. Chan, J. A. Evans, I.-K. Jang *et al.*, Nat. Med. **12**, 1429 (2006).

[51] See Supplemental Material at http://link.aps.org/supplemental/10.1103/PhysRevLett.132.233802 for a theoretical analysis of the proposed FMCW scheme, an implementation of the comb-calibrated method, a discussion about imaging resolution, comparisons with state-of-the-art NLOS methods, and additional experimental results, which includes Refs. [52–66].

[52] J. Zheng, *Optical Frequency-Modulated Continuous-Wave (FMCW) Interferometry* (Springer Science & Business Media, New York, 2005), Vol. 107.

[53] A. Vasilyev, The optoelectronic swept-frequency laser and its applications in ranging, three-dimensional imaging, and coherent beam combining of chirped-seed amplifiers, Ph.D. thesis, California Institute of Technology (2013).

[54] P. A. M. Sandborn, FMCW lidar: Scaling to the chip-level and improving phase-noise-limited performance, Ph.D. thesis, University of California, Berkeley, 2017.

[55] P. Lutzmann, B. Göhler, F. Van Putten, and C. Hill, *Electro-Optical Remote Sensing, Photonic Technologies, and Applications V* (2011), Vol. 8186, p. 11.

[56] P. Lutzmann, G. Anstett, and B. Göhler, in *Proceedings of the 15 th Coherent Laser Radar Conference, Toulouse* (2009).

[57] P. Rehain, J. Ramanathan, Y. M. Sua, S. Zhu, D. Tafone, and Y.-P. Huang, Opt. Lett. **46**, 4346 (2021).

[58] S. J. Rothberg, M. Allen, P. Castellini, D. Di Maio, J. Dirckx, D. Ewins, B. J. Halkon, P. Muyshondt, N. Paone, T. Ryan *et al.*, Opt. Lasers Eng. **99**, 11 (2017).

[59] L. Jia, Y. Wang, X. Wang, F. Zhang, W. Wang, J. Wang, J. Zheng, J. Chen, M. Song, X. Ma, M. Yuan, B. Little, S. T. Chu, D. Cheng, X. Qu, W. Zhao, and W. Zhang, Opt. Lett. **46**, 1025 (2021).

[60] G. Gorju, A. Jucha, A. Jain, V. Crozatier, I. Lorgeré, J.-L. Le Gouët, F. Bretenaker, and M. Colice, Opt. Lett. **32**, 484 (2007).

[61] X. Zhang, J. Pouls, and M. C. Wu, Opt. Express **27**, 9965 (2019).

[62] T.-J. Ahn, J. Y. Lee, and D. Y. Kim, Appl. Opt. **44**, 7630 (2005).

[63] E. Baumann, F. R. Giorgetta, I. Coddington, L. C. Sinclair, K. Knabe, W. C. Swann, and N. R. Newbury, Opt. Lett. **38**, 2026 (2013).

[64] J. L. Hall, Rev. Mod. Phys. **78**, 1279 (2006).

[65] T. W. Hänsch, Rev. Mod. Phys. **78**, 1297 (2006).

[66] Z. W. Barber, J. R. Dahl, T. L. Sharpe, and B. I. Erkmen, J. Opt. Soc. Am. A **30**, 1335 (2013).

[67] Q. Shen *et al.*, Nature (London) **610**, 661 (2022).

[68] T. Fortier and E. Baumann, Commun. Phys. **2**, 1 (2019).

[69] A. Lyons, F. Tonolini, A. Boccolini, A. Repetti, R. Henderson, Y. Wiaux, and D. Faccio, Nat. Photonics **13**, 575 (2019).

[70] N. Antipa, G. Kuo, R. Heckel, B. Mildenhall, E. Bostan, R. Ng, and L. Waller, Optica **5**, 1 (2018).

[71] B. Behroozpour, P. A. Sandborn, M. C. Wu, and B. E. Boser, IEEE Commun. Mag. **55**, 135 (2017).